ADVANCED ELECTRONIC MATERIALS Open Access
www.advelectronicmat.de

Copper Paste Printed Paper-Based Dual-Band Antenna for Wearable Wireless Electronics

Wendong Yang, Xun Zhao, Jingchang Nan, Michael Hengge, and Emil J. W. List-Kratochvil**

Wearable wireless electronics is becoming a significant research area because of the unique features of this technology. Within this field printed antennas are the key electrical component accomplishing the signal transmission and energy harvesting tasks and at the same these antennas need to be lightweight, environmentally friendly, safe to wear, and easy to conform. Currently, the majority of available paper-based antennas are designed for RFID, sensing, UWB, WLAN, and medical applications, with just a few being utilized in wearable applications, particularly for wireless body area network (WBAN). Furthermore, few studies have been conducted on the usage of printable copper conductive materials and low-temperature plasma technique for the fabrication of such antennas. This study demonstrates the realization of a dual-band paper-based wearable antenna by screen-printing of a plasma-sintered conductive copper paste. The copper paste, composed of 51 wt% solid particles, can easily produce desired conductive patterns on photo paper after printing and a subsequent plasma sintering, with a good adhesion. The antenna designed on photopaper operates in the frequency bands of 1.73–2.55 GHz and 7.66–8.89 GHz. Free-space simulation and measurement results reveal that the antenna exhibits stable radiation performance in the targeted WBAN (2.4–2.4835 GHz) and X uplink (7.9–8.4 GHz) frequency bands, together with low profile, excellent conformality and acceptable SAR values on the body and no electronic waste formed after disposal, making it a competitive candidate for usage in wearable wireless electronics.

1. Introduction

Wireless body area network (WBAN) systems have received widespread attention and interest for their versatile applications in health monitoring, telemedicine, military, sports, entertainment, search and rescue emergency operations.[1,2] Wearable antennas are the key component in the WBAN systems that provide wireless connectivity between wearable devices. The quality of the WBAN systems is largely determined by the performance of the antenna. Wearable antennas share many of the same requirements as traditional antennas, such as radiation performance including impedance bandwidth, radiation patterns, gain, polarization, etc.[3] However, it is also desirable for wearable antenna to be safe and easily conformable when put close to the human body.[4,5] In this way, wearable antenna can not only transmit/receive signals with high operating efficiency, but also keep the exposure of the human body to electromagnetic radiation, characterized by the specific absorption rate (SAR), below permissible limits.[6] In addition, to keep up with the trend of wearable devices, antennas should be lightweight, compact, and have high radiation efficiency, as well as steady performance, high flexibility, and ease of conformality, posing challenges for the structure design of the antennas.

In addition to structural design, recent advances in materials science and engineering open up new possibilities for wearable antennas. Low-cost materials and simple low temperature manufacturing procedures are becoming the focus of the antenna designers. Paper-based antennas become a popular topic due to their unique characteristics of lightweight, eco-friendly, biodegradable and flexible.[7] Paper-based antennas can be fabricated using a simple process thanks to advances in printed electronic technology.[8,9] Because of the distinctive surface of paper materials and their inability to endure extreme temperatures, conductive materials that are compatible with the paper materials and can be processed at low temperatures have become the key materials for paper-based antennas.

At present, a variety of paper-based antennas have been developed using printed electronic technology.[10–18] Gheethan et al.[10]

W. Yang, E. J. W. List-Kratochvil
Department of Physical and Chemistry
Humboldt-Universität zu Berlin
12489 Berlin, Germany
E-mail: yangwendong@lntu.edu.cn; emil.list-kratochvil@hu-berlin.de
W. Yang, X. Zhao, J. Nan
School of Electronic and Information Engineering
Liaoning Technical University
Huludao 125105, China
W. Yang, M. Hengge, E. J. W. List-Kratochvil
Helmholtz-Zentrum Berlin für Materialien und Energie GmbH
14109 Berlin, Germany
The ORCID identification number(s) for the author(s) of this article can be found under https://doi.org/10.1002/aelm.202400522

DOI: 10.1002/aelm.202400522

developed an inverted F-antenna that operates at 2.45 GHz on a paper substrate, demonstrating its feasibility for wireless local area network (WLAN) applications. The antenna was designed and direct-write printed on a paper substrate with a silver conductive ink. Shaker et al.[11] demonstrated the feasibility of realizing ultra wide band (UWB) antennas with frequencies over 10 GHz through inkjet-printing of conductive ink on commercial paper sheets. The properties of paper substrates were studied with bifurcated dielectric resonator technology. Leng et al.[12] developed a low-profile meandered-line dipole antenna made of graphene nanosheets on a paper substrate with screen printing. The proposed antenna provides practically acceptable radiation properties for mid-and short-range radio frequency identification (RFID) and sensing applications. Gonzalez-Perez et al.[14] reported a 24 GHz paper-based Yagi–Uda antenna with a bowtie director. Compared to the traditional Yagi–Uda antenna, the innovative bowtie director introduced increased the bandwidth of the antenna by 240 % while increasing the gain bandwidth increase by three times. The antenna is suitable for low-cost, eco-friendly and flexible wireless applications. Abutarboush et al.[16] demonstrated a frequency-reconfigurable inkjet-printed antenna on a commercial photopaper substrate. Two pin diodes were employed to realize the switch between the main radiator and the L- and U-shaped radiators, allowing the antenna to operate in different frequency bands. Simulation and measurement results revealed that the antenna had a stable radiation pattern and moderate gain throughout all operating frequency bands. Shyam et al.[17] presented a paper-based flexible antenna for an intrabody telemedicine applications. The antenna operates in the 2.4 GHz industrial, scientific, and medical radio frequency bands and has a high level of flexibility and gain.

Despite advances have been made in the development of paper-based antennas, there are still some limitations. To begin, the present paper-based antennas are mostly created for RFID,[12,15,19,20] sensing,[21] UWB,[11] WLAN,[10] and medical applications,[17] with few being used in the wearable field, particularly for WBAN systems. As for the reason, it may be related to the fact that these applications do not need to withstand long-term and multiple deformation, and some of them are disposable such as the usage in patches. For instance, paper-based antennas tailored for UWB and WLAN applications are often used in fixed or semi-fixed environments with relatively low physical durability requirements. Second, there have been few reports on the usage of printable copper conductive materials in the development of paper-based antennas. Silver nano-ink[22–26] or silver nano-paste[27–29] are the most often utilized materials. Compared to silver, copper-based conductive inks or pastes are less expensive, yet offer comparable conductivity.[30] However, oxidation issues during preparation, storage, post-treatment and application are matters to consider with copper inks or paste.[31,32] Finally, thermal sintering is frequently adopted to activate the printed antenna patterns and make them conductive, whereas alternative sintering approaches,[33] such as photonic sintering,[34–38] plasma sintering[39,40] and microwave sintering,[41,42] are seldom explored. Plasma sintering can quickly realize the sintering of conductive materials at lower temperatures and reduce thermal damage to the substrate, making it a promising method for paper-based applications. Therefore, it will be interesting to explore the application potential of plasma-activated copper materials in the fabrication of printed paper-based wearable antennas.

In this paper, we demonstrate the feasibility of realizing a dual-band wearable antenna through screen-printing of a plasma-sintered copper paste on commercially available photopaper. The dielectric and surface properties of the selected photopaper material, as well as the thermal, printing, and electrical properties of the adopted copper paste, were investigated thoroughly first to ensure the feasibility of designing and printing antenna patterns on photopaper substrates. Then, a wearable antenna of 38 mm × 24 mm × 0.27 mm was designed and screen-printed with the copper paste on photopaper, which exhibits good dual-frequency resonance characteristics in the targeted WBAN (2.4–2.4835 GHz) and X uplink (7.9–8.4 GHz) bands, as well as excellent conformality and acceptable SAR values on the body, making it a viable candidate for flexible or wearable wireless electronics.

2. Antenna Structure Design

The paper-based antenna proposed was designed to operate in the WBAN and X uplink frequency bands for wearable applications. The required dielectrical parameters of the inkjet photopaper substrate were determined using a resonator method, as detailed in Section 4.1.

A rectangular monopole antenna with a coplanar waveguide (CPW) feed structure was chosen as an initial design structure, named as Ant1 (**Figure 1a**). Although Ant1 operates effectively at high frequencies (8.5 GHz), its reflection coefficient at 2 GHz does not fulfill design requirements (Figure 1b). It also doesn't cover the desired WBAN frequency band. Therefore, we optimized the structure of Ant1. By sequentially adding an isosceles triangle with an angle of 56.5° to the top of the radiation patch of Ant1, reducing the width of Ant1's ground plate (Ant2), and introducing a gradient feeder structure on Ant1 (Ant3) successively, the final antenna structure was obtained.

As shown in Figure 1d, the optimized antenna consists of a radiation patch with an isosceles triangle and rectangle, a gradient CPW feed structure, and a pared-down ground plate. This design was chosen to address both low- and high-frequency impedance matching, ensuring broad bandwidth performance. The combination of the isosceles triangle and rectangle in the radiation patch allows for the tuning of dual-frequency resonances, while the gradient CPW feed structure enhances impedance matching across the frequency bands. The dimensions of the antenna were finalized based on theoretical analysis and simulation results from Ansys HFSS software to ensure that the antenna has good dual-band response characteristics and impedance matching within the targeted frequency ranges of 1.73–2.55 GHz and 7.66–8.89 GHz. The placement of both the radiation patch and ground plate on the same side of the substrate facilitates the screen-printing process, making the manufacturing of the antenna more efficient.

The optimized antenna structure not only addresses the low-and high-frequency impedance matching problem, but it also assures the antenna's broadband performance to meet the design requirements. The ultimate antenna dimensions were

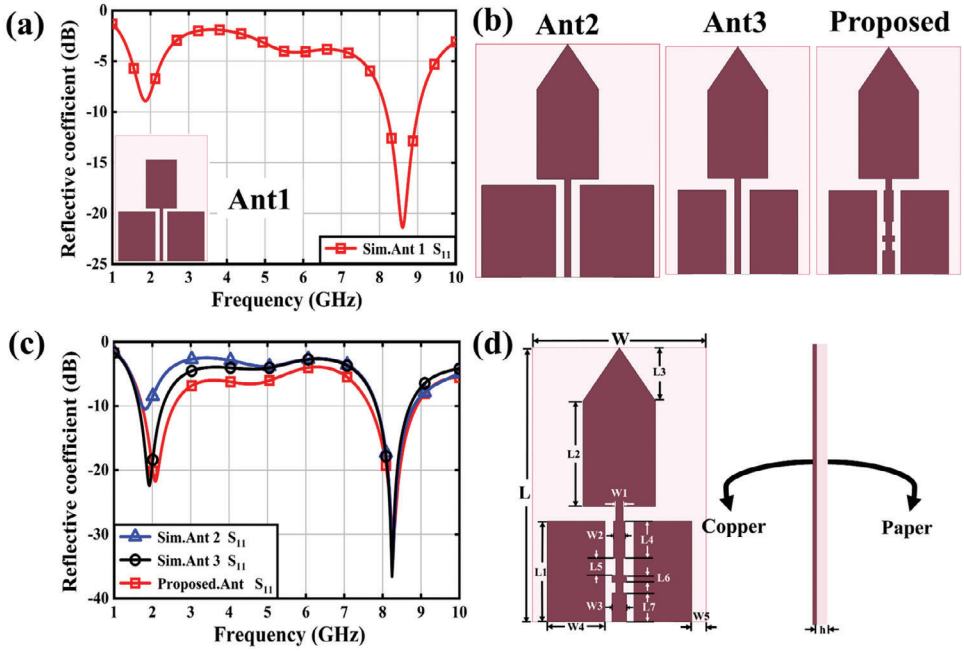

Figure 1. a) Front view of the initial rectangular microstrip patch antenna and its reflection coefficient; b) Evolution stages of the antenna structure design; c) Reflection coefficient corresponding to each stage; and d) Front and side view of the optimized antenna.

Table 1. Dimensions of the optimized antenna (Units:mm).

Parameter	Value	Parameter	Value	Parameter	Value
L	38	L4	5.2	W1	1
W	24	L5	2.3	W2	1.6
L1	14	h	0.27	W3	2
L2	14.6	L6	1	W4	8
L3	7.3	L7	4	W5	2

38 mm × 24 mm × 0.27 mm, and the values for each parameter are listed in **Table 1**.

3. Antenna Fabrication

3.1. Materials and Methods

The proposed paper-based antenna was fabricated utilizing a commercial conductive copper paste, Delo-3310 (Shenzhen Delo Technology Development Co., Ltd., China). The paste has a high viscosity of 20–30 Pa·s and contains 50–65 wt% solids. All printing experiments were carried out on a screen printer (Shenzhen Delo Technology Development Co., Ltd., China) with a 250-mesh screen. During the experiment, the smallest resolution that could be produced by the screen-printing was 0.3 mm. As for the antenna pattern, we printed it three times to ensure optimal electrical performance and print quality. Thermal or plasma sintering was employed to process the printed samples. Thermal sintering was performed for 60 min in an oven at temperatures ranging from 130 °C to 170 °C. The plasma sintering was carried out for 5–30 min using a low-pressure argon plasma equipment with a power output of 180–300 W.

3.2. Characterization

The thermal decomposition behaviors of the copper paste were investigated using a simultaneous thermal analyzer (DSC-TG, HITACHI STA200) and aluminum pans in a nitrogen atmosphere. Samples were heated from 30 °C to 300 °C at a rate of 10 °C per minute. The phases, morphologies and chemical composition of sintered copper films were determined using X-ray diffraction (XRD, Rigaku, Cu Ka radiation, k = 0.15418 nm) measurement, scanning electron microscope (SEM, ZEISS Gemini 300), and surface energy disperse spectrometer (EDS, Oxford Xplore30), respectively. The sheet resistance of the sintered copper films was measured with a four-point probe analyzer. The reflection coefficient and bending performance of the antenna prototype were investigated using a vector network analyzer (Ceyear 3674H) and Prtronic Flexible Electronic Tester (FT2000, Shanghai Mifang Electronic Technology Co., Ltd., Shanghai, China). A human arm and a multilayer human tissue phantoms were employed to validate on-body performance of the fabricated antenna prototype, separately.

4. Results and Discussion

4.1. Dielectric and Surface Properties of Paper Substrate

Paper is generally composed of cellulose fibers,[43] but the properties of each paper type vary due to differences in material compositions and production processes. Inkjet photopaper is an image printing paper with a special coating that aids in the absorption of ink or paste materials. This coating is usually composed of materials such as silica, alumina forms, titanium dioxide, calcium carbonate, and various polymers. The special treatment of the photopaper makes it more supple, stable and smooth than

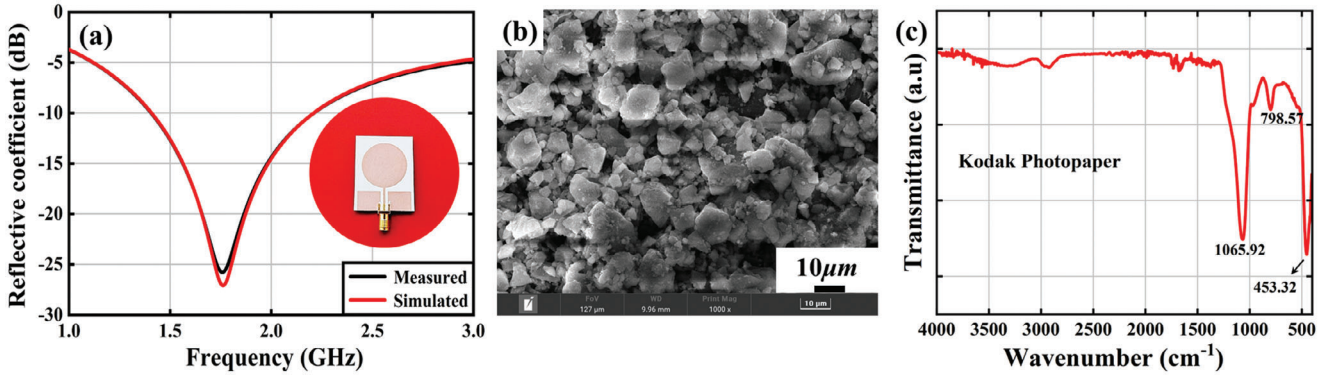

Figure 2. a) Dielectric constant measurement of photo paper using the resonator method, b) Surface morphology and c) FT-IR results of the photo paper material.

normal paper. It also means that the ink or paste is not immediately absorbed, resulting in a high print quality. Basically, photopaper is available in matte, satin and glossy. Here, a Kodak matte inkjet photopaper (A4, 210 mm × 297 mm, Resin Coated) was chosen as the substrate of the antenna. This type of matte photopaper was chosen as the substrate for the antenna primarily because it has a lower surface reflectivity than satin or glossy papers. It provides a non-reflective surface that reduces undesired reflections and signal interference, which is crucial for accurate antenna performance. Additionally, this matte photopaper tends to have better adhesion properties for the copper paste used in antenna fabrication, ensuring more consistent and reliable electrical performance as well as robust antenna performance.

Considering that the simulation of antenna structure requires the dielectric parameters of the substrate material, and the fabrication of the antenna prototype requires appropriate conductive materials and patterning techniques that are compatible with the photopaper substrate, the dielectric and surface properties of the selected photopaper material were studied. A resonator method was adopted to determine the dielectric constant of photo-paper.[44] The basic principle of this approach is to create a microstrip antenna on the material to be measured with an assumed dielectric constant value, and use a network analyzer to determine the resonance point of the antenna. Then, the calculation formula of the microstrip antenna is used to acquire the accurate dielectric constant value of the measured material.

In the study, a CPW-fed circular monopole antenna operating at 1.4–2.21 GHz was designed using the photopaper with an assumed dielectric constant value of 2.5. Then, an antenna prototype was fabricated on photopaper and its resonance point was measured using a vector network analyzer, as shown in **Figure** 2a. By adjusting the dielectric constant in HFSS software to let the simulated reflection coefficient close to the measured one, the dielectric constant of the photopaper base material was eventually determined to be 3.2. This value is consistent with the one provided in the ref. [45], which is important for the structural simulation of subsequent paper-based antenna.

In addition to the dielectric properties, we also investigated the surface properties of the photopaper. Figure 2b shows the surface morphology of the selected photopaper material. The photopaper has a surface structure composed of pores and particles of different sizes, with large pores between the particles and fine pores inside the particles. According to ref. [46], this is an interesting structural feature of the synthetic silicas: they have a large internal surface area caused by micro-pores within the particle. However, this is unfavorable for the application of low-viscosity conductive ink, because it is difficult to form a uniform film, and it can also easily result in the lack of a clear film/substrate interface between the electrical functional layer and the substrate, which seriously affects the electromagnetic and mechanical properties and geometry of the printed antenna pattern. Therefore, choosing the appropriate printing material is crucial to produce antenna prototypes.

FT-IR was employed to investigate the active groups on the surface of the photopaper, and the result was given in Figure 2c. A sharp absorbance peak and a weak absorbance peak appear at 1065.92 cm^{-1} and 798.57 cm^{-1}, which may be caused by particles in the surface coating of the photopaper, as observed by SEM and confirmed by later XRD analyses. According to the peak position, we infer that these peaks are likely from the Si–O vibrations of silicon dioxide since the stretching, bending, and rocking vibrations of Si–O bond appear at 1080 cm^{-1}, 800 cm^{-1}, and 450 cm^{-1} respectively.[47,48] The presence of such a silicon dioxide coating will cause the ink or paste to be drawn deep into the layer by capillary action, resulting in its quick dry on the surface of the photo paper, which is conducive to generating fine patterns. The above analyses provide a preliminary understanding of the photopaper's dielectric and surface properties, which is the basis for the subsequent antenna design and printing material selection.

4.2. Thermal Behavior and Printability of Copper Conductive Paste

Copper paste, like most conductor pastes, consists of three components: the conductive phase (copper particles), the binding phase and organic additives.[49,50] It is a dispersion of solid particles in organic vehicles. For screen printing, the viscosity of conductive paste impacts the quality of the printed pattern. If the viscosity is too high, it will be difficult for the paste to transfer to the substrate, and blockage will easily occur. If the viscosity is too low, the paste will be very fluid. The imprint of the pattern expands and the printing accuracy decreases. In addition, the surface tension of the paste and the surface energy of the substrate

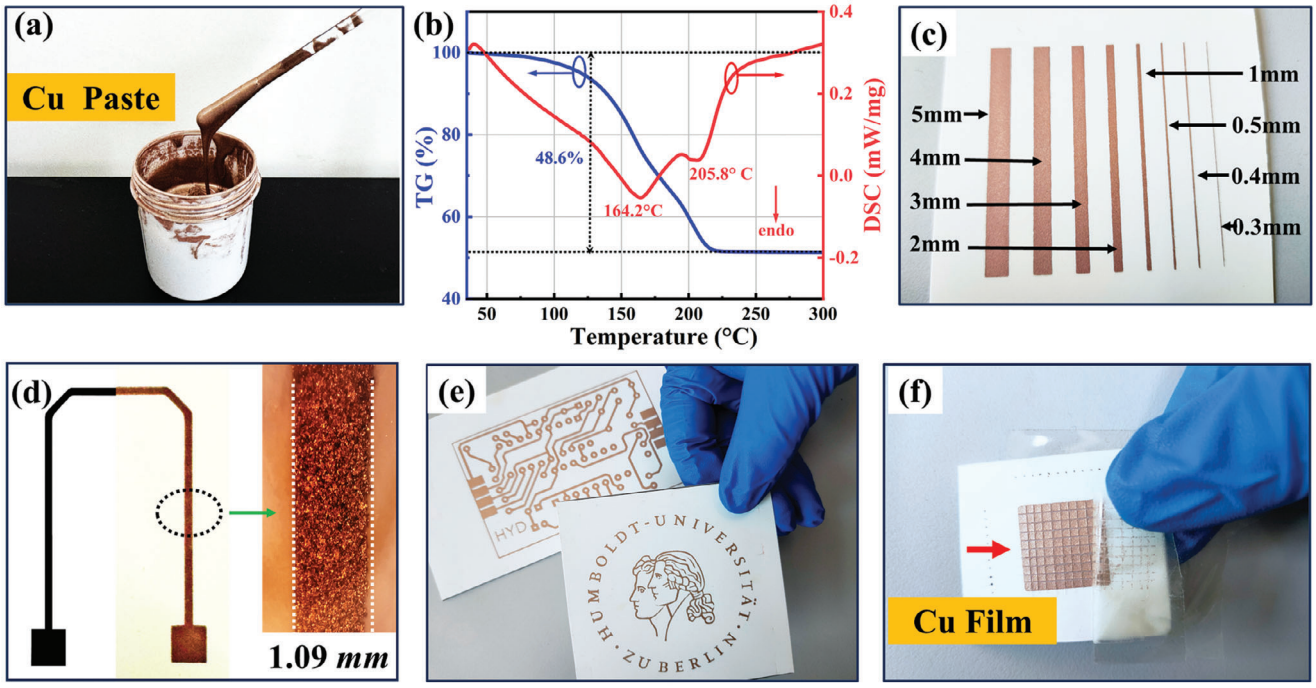

Figure 3. a) Optical image and b) DSC-TG results of the selected copper paste, c,d,e) Screen-printed lines and patterns on photopaper substrates, and f) adhesion test of the screen-printed copper film.

are also factors that need to be considered, because they determine the wettability of conductive paste on the substrate. Therefore, choosing a copper paste with appropriate physicochemical properties is critic for the latter patterning process. After careful consideration, a commercial copper conductive paste that has good printability, electrical conductivity, oxidation resistance and bendability was employed here for the screen-printing of the designed antenna.

As shown in **Figure** 3a, the paste is red-brown in color and composed of copper particles, organic vehicles and additives. It has a viscosity of 20–30 Pa·s and does not require diluting before use. It is suited for mesh printing from 100 to 200 and has some oxidation resistance. DSC-TG, rheometer and optical microscope analyses were employed to examine its thermal decomposition behavior, fluid properties and printability.

The TG curve in Figure 3b reveals a two-step weight loss from 30 °C to 220 °C. The first weight loss from 30 °C to 180 °C, featured by an endothermic peak at 164.2 °C on the DSC curve, is attributed to the evaporation or/and decomposition of organic solvent and additives in the copper paste. The second weight loss from 180°C to 250 °C is caused by the aggregation and coalescence of the copper particles, as well as the continued decomposition of the organic matters, which corresponds to an endothermic peak at 205.8 °C on the DSC curve. The remaining weight is about 51.4 wt%, which is comparable with the value provided by the supplier. DSC-TG results reveal that a temperature higher than 170 °C is required for the sintering of copper paste, and the sintering products include some organic matters in addition to copper particles.

The printing of the copper paste was conducted on plasma-treated photopaper substrates with a screen printer. During printing, the number of layers were carefully chosen to ensure accurate printing dimensions and good conductivity. As shown in Figure 3c–e, lines with various widths and patterns were successfully screen printed and thermal-sintered on photopaper substrates, indicating that the paste has a good printability. When the width of the line was set to be 1.0 mm, the obtained copper conductive line has a width of 1.09 mm (Figure 3d), basically the same, indicating a favorable printing accuracy. The adhesion test results in Figure 3f show that the copper paste has good adhesion (4B) after printing and thermal sintering. The above results indicate that the selected copper paste has good screen-printability and excellent film-forming capability on the used photopaper.

4.3. Electrical Performance and Microstructures of Printed Copper Films

4.3.1. Electrical Properties

The printed film needs to be sintered to create a dense structure and improve conductivity. Thermal sintering is one of the commonly used sintering methods. However, for paper-based substrates, a higher temperature will damage their surface. Plasma sintering can achieve high-quality sintering at lower temperatures in a shorter time,[51,52] making it suitable for the application with paper-based substrates. At the same time, the plasma sintering can improve the adhesion between the copper paste and the substrate material, therefore it is adopted here.XRD and XPS analyses were employed to investigate the physical composition and surface chemical state of the copper

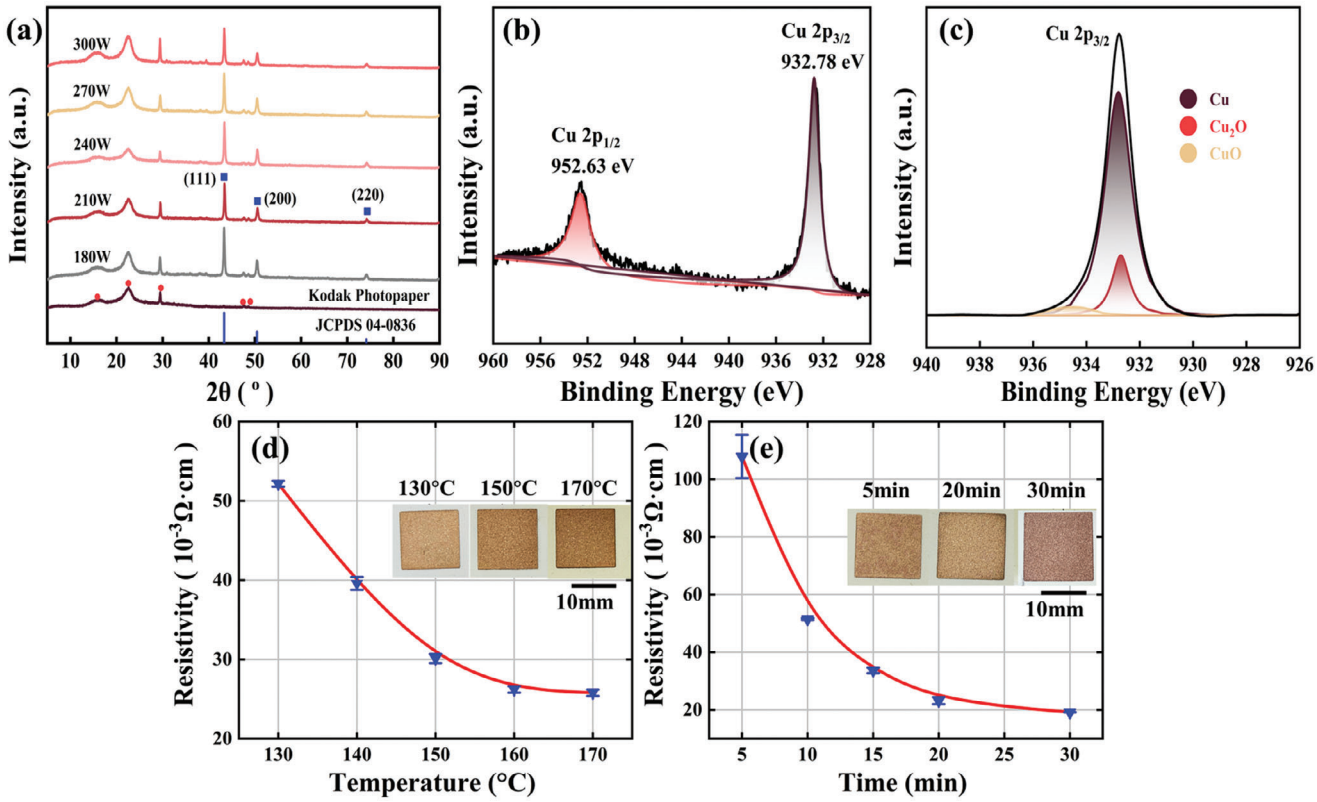

Figure 4. a) XRD results of copper films sintered at different plasma power for 30 min, b,c) XPS results of copper film sintered at 300 W for 30 min, d) Resistivity of copper films sintered at different temperatures for 60 min and e) at 300 W for different times.

films. **Figure** 4a shows the XRD spectrum of the copper films sintered at different plasma power. Three diffraction peaks at 43.3°, 50.4° and 74.1° are found in all the films, which correspond to the characteristic values of metallic copper, indicating that the sintered films are composed of copper. Given the limitations of XRD in detecting amorphous oxides, XPS analysis was performed to confirm the presence of copper oxides in the sintered films. Figure 4b shows the spectrum analysis of Cu 2p1/2 and Cu 2p3/2 at 952.63 eV and 932.78 eV respectively. As seen, there are some weak satellite peaks. Further peak split fitting on the Cu 2p3/2 peak (Figure 4c) indicates that the film is mostly composed of elemental Cu and a small amount of Cu_2O.

A four-point probe system were used to investigate the electrical performance of the sintered copper films against plasma time or temperature. As shown in Figure 4d,e, the resistivity of the film decreases with increasing time or temperature. For plasma sintering, it decreases from 107.88 ± 7.49 μΩ cm to 19.17 ± 0.04 μΩ cm after 30 min, and for thermal sintering, it decreases from 52.15 ± 0.37 μΩ cm at 130 °C to 25.79 ± 0.4 μΩ cm at 170 °C.

The decrease in resistivity with temperature or time is easily understood since organic matters mostly evaporate or/and decompose, and copper particles are better connected. In comparison with thermal sintering, plasma sintering achieves comparable electrical performance in less time, as proved by resistivities obtained at 150 °C for 60 min (30.11 μΩ cm) and 300 W for 15 min (33.68 μΩ cm). Besides, plasma sintering can yield lower resistivity than thermal sintering without damaging the substrate. For photopaper substrates, excessively high sintering temperatures, such as 170 °C, will damage the surface and result in a yellow surface; however, plasma sintering can avoid this due to its short processing time. Based on the optical images of the copper film under different sintering conditions and the electrical performance requirements of the antenna, 300 W and 30 min were finally chosen as the optimal sintering parameters. Here, higher plasma power will result in shorter processing times, however due to instrument limitations, this is our only option.

4.3.2. Surface Morphologies

Figure 5a,b shows the surface morphologies of copper films after thermal sintering (170 °C, 60 min) and plasma sintering (300 W, 30 min, argon atmosphere), respectively. Both copper films, the morphology of copper particles is flake-like. These flakey particles are stacked in a laminated manner and close contact with each other. In comparison to thermal-sintered copper film, the plasma-sintered film is composed of larger copper flakes with good connections and are more uniform and denser. Additionally, there are fewer voids and gaps in the film. This structure is conducive to obtaining good electrical properties, which has been confirmed by previous analyses.

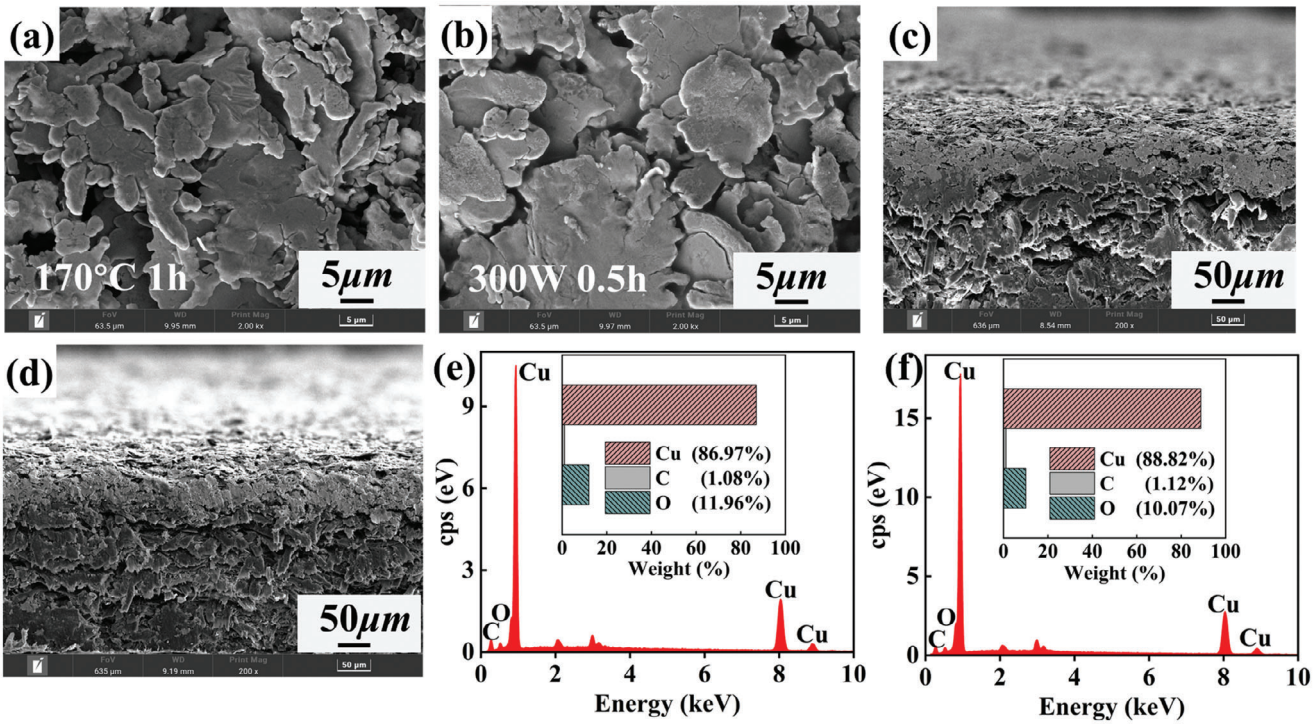

Figure 5. Surface and cross-sectional morphologies as well as EDS results of the screen-printed copper films sintered a,c,e) at 170 °C for 60 min and b,d,f) 300 W for 30 min.

The cross-section images in Figure 5c,d show that the average thickness of the film produced from thermal sintering was about 53.20 ± 2.90 μm, and 51.74 ± 0.51 μm for plasma sintering. Furthermore, plasma sintering behavior has stronger cross-sectional behavior than thermal sintering, as evidenced by the degree of accumulation of copper flake particles. Moreover, the surface of the film layer is flatter. EDS spectra of both copper films are given in Figure 5e,f. As seen, Cu, O, and C elements are present in the films, and the mass proportions of copper in both films are 86.97 wt% and 88.82 wt% respectively. This means that the films have some organic residues in addition to the metal copper. EDS results also demonstrate the feasibility of using plasma technology to prepare conductive copper films on heat-sensitive paper substrates.

Generally, the electrical properties of plasma sintered copper films are influenced by several key factors, including the film's microstructure, grain size, porosity, and sintering quality. A smaller grain size and lower porosity typically result in lower resistivity due to better particle connectivity and electron flow. Plasma sintering parameters, such as power, pressure, and duration, also play a critical role, as they affect the densification and bonding between particles. Additionally, the purity of the copper and the presence of any impurities or oxidation during the sintering process can impact the film's conductivity. Controlling these factors is essential for optimizing the electrical properties of the sintered copper films.

Overall, the film obtained by plasma sintering is superior to thermal sintering in terms of grain size, morphology and density.

4.4. Antenna Performance

4.4.1. Radiation Properties

The radiation characteristics and surface current distribution of the proposed antenna were simulated with Ansys Electronics 2023 R2 software. **Figure 6a,b**, show the simulated radiation patterns of the proposed antenna at 2 GHz and 8.2 GHz. The antenna exhibits uniform radiation performance in the horizontal direction and omnidirectional radiation characteristics. When the antenna operates at 2 GHz, the E-plane radiation pattern resembles a figure "8" while the H-plane pattern is circular. The radiation patterns at 8.2 GHz are like the result at 2 GHz but with slight distortion associated with the physical size of the antenna. In general, higher frequencies will make the antenna size larger relative to the wavelength, thereby causing changes in the radiation pattern.

Figure 6c,d shows the surface current distribution of the antenna at 2 and 8.2 GHz. Clearly, the majority of the current is concentrated around the feed line, which indicates that the gradient feed line effectively couples energy into the antenna, prompting a good impedance match, so that the antenna can be effectively excited at different frequencies. This highlights the advantages of adopting a gradient feed line structure in design.

The antenna prototype was tested to verify the reliability in design (**Figure 7a,b**). The reflection coefficient was measured using a Ceyear (3674H) vector network analyzer. As shown in Figure 7d, the measured reflection coefficient is basically consistent with the simulation results, especially at 8.2 GHz. At 2 GHz, the values

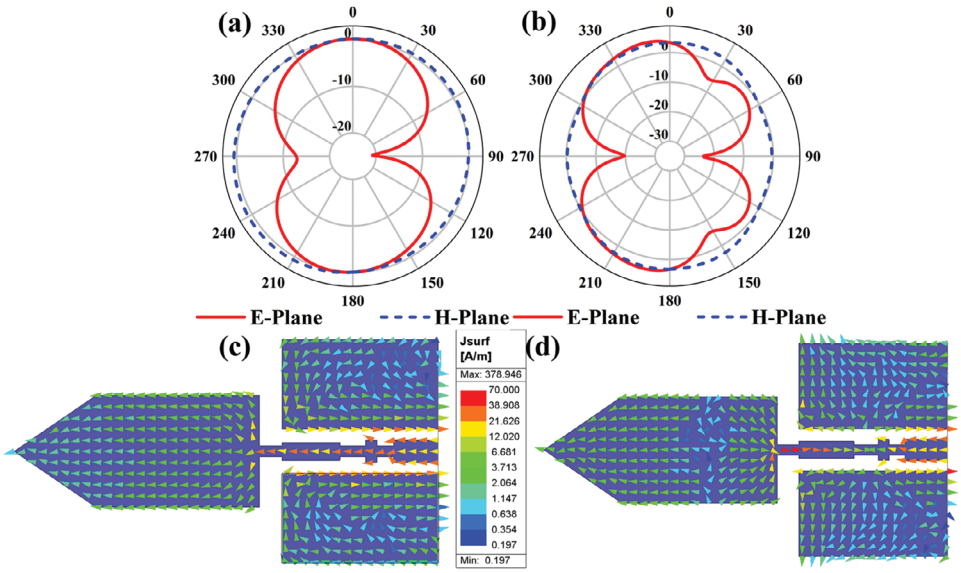

Figure 6. The simulated radiation patterns and surface current distribution of the proposed antenna at a,c) 2 GHz and b,d) 8.2 GHz.

have a slight difference with the simulated ones, accompanied by an upward resonance point.

The radiation patterns of the antenna prototype at 2 and 8.2 GHz were obtained in an anechoic chamber using an Agilent E4446A spectrum analyzer and Agilent N8183A RF signal generator, and the results are given in Figure 7e,f. As seen, the radiation patterns of the antenna match well with the simulation results, demonstrating the reliability in simulation. Gain values were measured at the main lobe direction $\theta = 270°$, with a value of 0.67 dB at 2 GHz and 3.21 dB at 8.2 GHz, respectively, slightly deviating from the measured results but in an acceptable range. This discrepancy may be attributed to the lower copper content in the printed copper pattern.

On the whole, the measured results verify the rationality of the antenna in the simulation, and the designed antenna exhibits good omnidirectional radiation characteristics and wideband matching performance in performance indicators.

4.4.2. Wearability

Wearable devices frequently have to withstand deformations caused by the human; therefore, the antenna needs to be flexible and bendable to maintain stable performance. For wearable antennas, they should be designed to withstand deformation while being safe to wear. This is because the antenna works in an environment close to the human body, if the radiation is too strong or the material is improperly selected, it may have an impact on human health. In this section, the bendability and wearability of the designed antenna were investigated respectively.

1) Bendability

Conformality is an important criterion when evaluating wearable antennas. Antennas that are more conformable will be easier to integrate into wearable device systems. Figure 7g shows the measured reflection coefficients of the antenna at bending radii ranging from 5 to 20 mm with a step of 5 mm along the Y-axis. As seen, when the bending radius exceeds 5 mm, the antenna's reflection coefficient changes very little, and continues to function well within the frequency band. However, as the bending radius reaches 5 mm, the bandwidth of the antenna's reflection coefficient at high frequencies broadens, allowing more signals to be received and impacting the reception of the target signal. When the bending radius is less than 5 mm, the performance of the antenna decreases. These results indicate that the antenna has excellent bendability when the bending radius is greater than 5 mm.

A cyclic bending test was performed on the fabricated antenna prototype to study the change in resistivity after bending (Figure 7h). The results show that within 10 000 cycles, the resistivity of the antenna changes very little, demonstrating the antenna's longevity.

Usually, bending an antenna can significantly impact its performance, particularly affecting parameters such as impedance, gain, and radiation pattern. When an antenna is bent, it can cause changes in the effective length of the conductive path, which may lead to a shift in resonance frequency and altered impedance matching. Additionally, bending can introduce mechanical stress, which might affect the integrity of the conductive layer and the substrate, potentially leading to degradation in electrical performance. For a dual-band antenna, the shift in resonance frequency under bending conditions is typically more pronounced at the high-frequency end compared to the low-frequency end, this is especially true in our case. As for the reason, it is because high-frequency resonators are more sensitive to changes in dimensions. As the antenna is bent, the effective length and shape of the high-frequency resonator are altered more significantly, leading to a greater shift in its resonance frequency. One should be mindful of these factors when selecting materials and designing flexible antennas, as the choice of

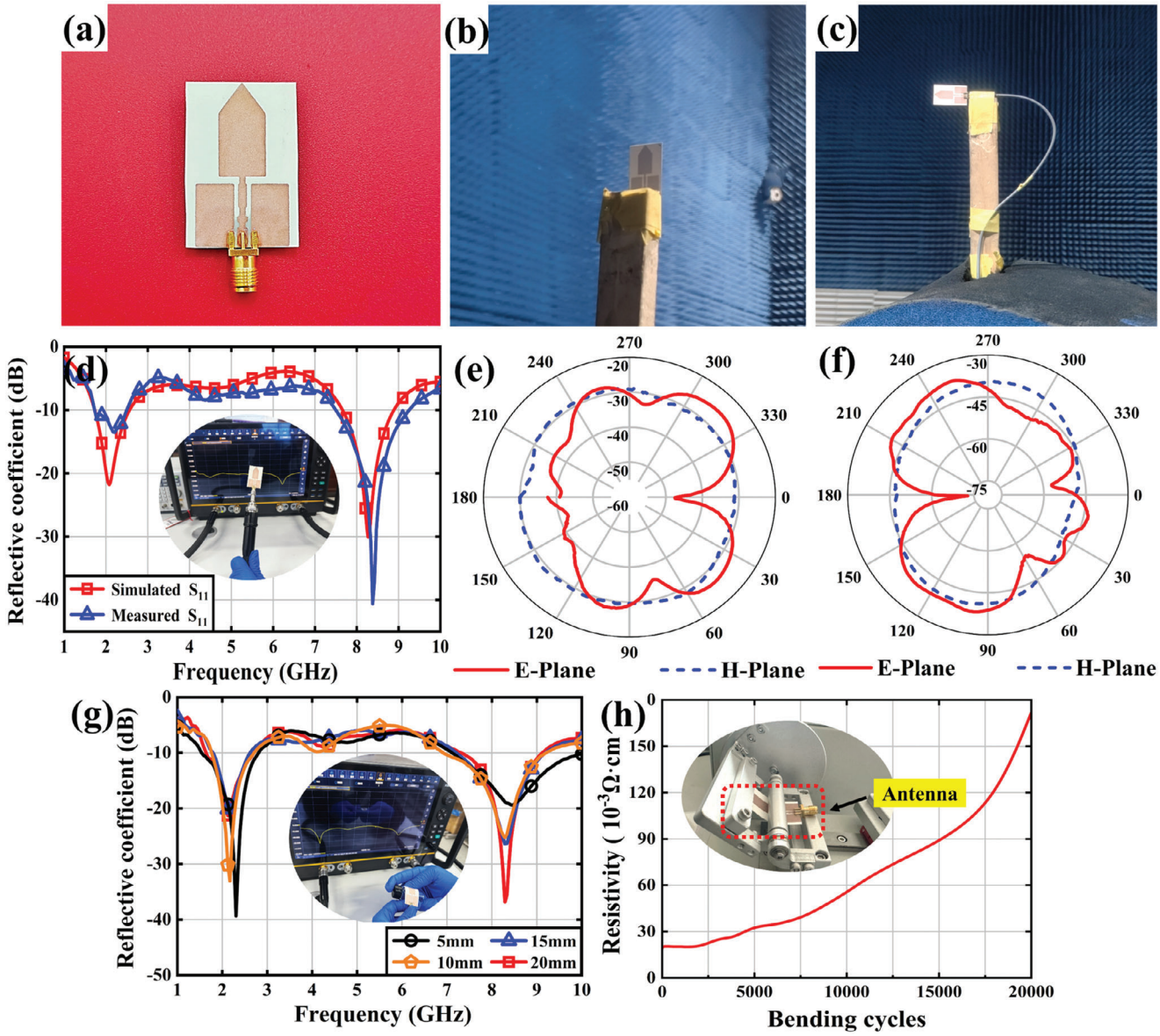

Figure 7. a) The fabricated antenna prototype, b,c) test in an anechoic chamber, d) the measured reflection coefficient and e,f) radiation patterns at 2 and 8.2 GHz, g) the reflection coefficients against bending radii and (h) the change in resistivity after bending.

substrate and conductive materials needs to accommodate bending without compromising the antenna's functionality.

2) Wearable Safety

Specific absorption rate, SAR, is an important parameter to the wearable antenna. The SAR value is used to evaluate the antenna security performance for wearable applications. It is defined as the power absorbed per mass of tissue (W kg^{-1}) and can be calculated using the following Equation (1).

$$SAR = \frac{\sigma |E|^2}{\rho} \quad (1)$$

Where σ is the conductivity of human tissue in S m^{-1}, E is the electric field in V m^{-1}, and ρ symbolizes the mass density of human tissue in kg m^{-3}.

To protect the users from hazardous RF exposure, the SAR must not be greater than 1.6 W kg^{-1} per 1g of tissue for US standard and no more than 2 W kg^{-1} per 10 g of tissue for EU standard. Only when the test results meet these standards can the designed antenna be deemed safe to wear.

A 90 mm × 90 mm × 33 mm planar three-layer human arm model, composed of skin (2 mm), fat (8 mm), and muscle (23 mm) layers, was built on Ansys HFSS simulation software to investigate the SAR level of the antenna, as shown in **Figure** 8a. The dielectric properties required for each layer at 2 and 8.2 GHz are listed in **Table** 2. For the off-body measurements, the antenna

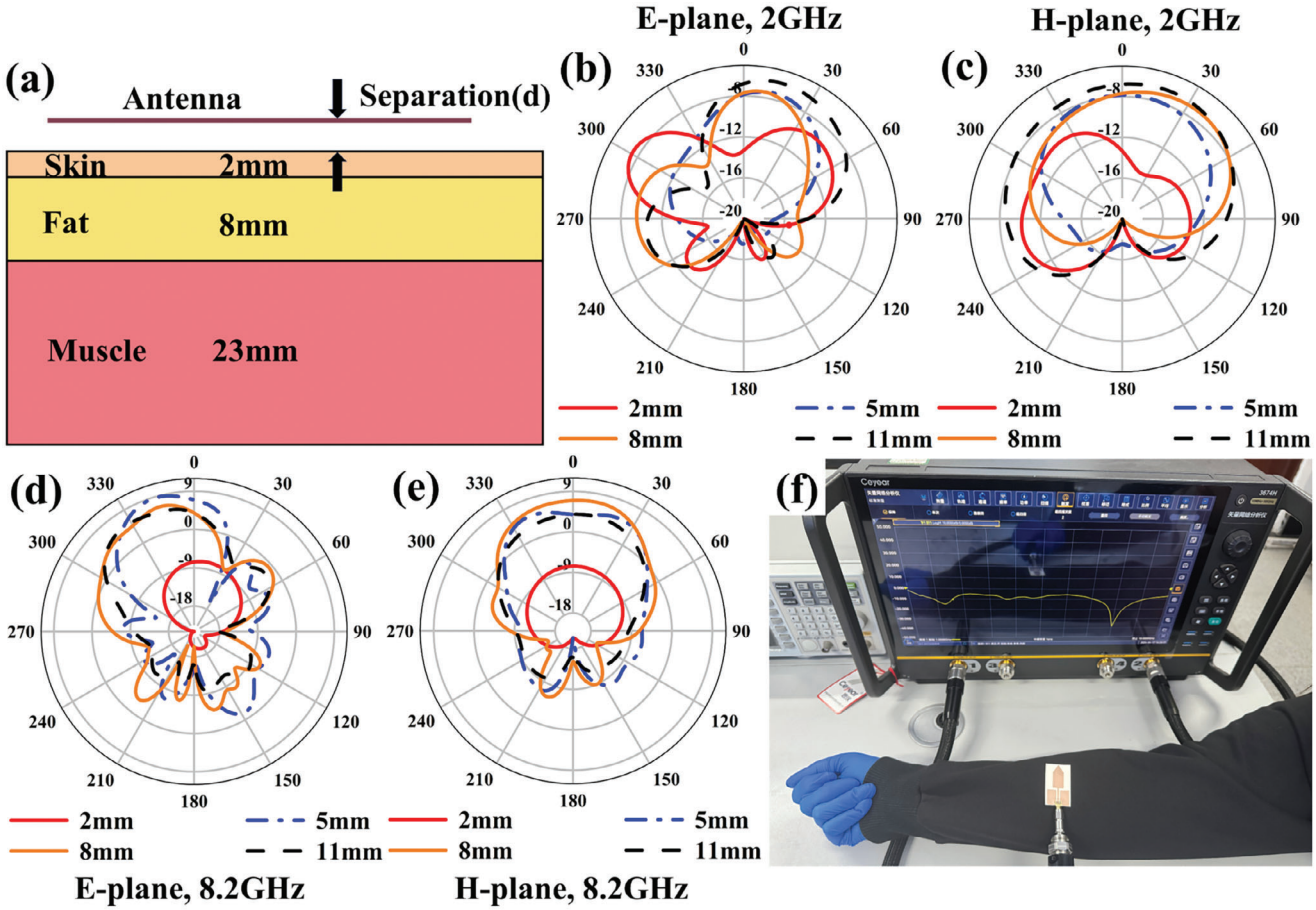

Figure 8. a) The three-layer human arm model, the E-plane and H-plane radiation patterns of the antenna distanced by various "d" values at 2 GHz b,d) and 8.2 GHz c,e), and f) reflection coefficient at a "d" value of 5 mm.

Table 2. Human tissues dielectric characteristics at 2 and 8.2 GHz.

Human Tissue at 2 GHz	Skin (dry)	Fat	Muscle (Transverse Fiber)
Relative Permittivity	38.568	5.3276	53.29
Conductivity (S m^{-1})	1.2654	0.085918	1.4538
Loss tangent	0.29489	0.14494	0.2452
Mass Density (Kg m^{-3})	1090	930	1050

Human Tissue at 8.2 GHz	Skin (dry)	Fat	Muscle (Transverse Fiber)
Relative Permittivity	32.999	4.7455	45.223
Conductivity (S m^{-1})	6.0337	0.45709	8.0727
Loss tangent	0.40081	0.21115	0.39132
Mass Density (Kg m^{-3})	1090	930	1050

was placed on the top of the mode with a separation distance of "d."

The SAR levels of the antenna at frequency points of 2 and 8.2 GHz were examined with different "d" values and 100 mW as input power. The results are given in **Table 3**. When the separation distance "d" is 5 mm, the power consumption is 1.3 and 0.287 W kg^{-1} at 2 GHz, and 1.446 and 0.301 W kg^{-1} at 8.2 GHz.

Table 3. SAR levels, Gain and Efficiency of the proposed antenna at 2 and 8.2 GHz with different separation distance.

Separation Distance [mm]	Frequency [GHz]	1g/10g	Max. SAR [W kg^{-1}]	Gain [dBi]	Total Efficiency [dB]
2	2	1g	2.168	−7.3818	−2.60142
		10g	0.528		
	8.2	1g	4.217	2.25746	−3.68009
		10g	0.948		
5	2	1g	1.3	−7.07312	−3.2994
		10g	0.287		
	8.2	1g	1.446	−1.47141	−1.47141
		10g	0.301		
8	2	1g	0.734	−7.34974	−2.64526
		10g	0.155		
	8.2	1g	0.735	8.76179	−1.485447
		10g	0.152		
11	2	1g	0.402	−6.24153	−1.0188
		10g	0.082		
	8.2	1g	0.535	5.59675	−1.29606
		10g	0.105		

These values are below the SAR limits of the US or EU safety standards, indicating that the antenna is safe to wear.

We also investigated the antenna's radiation performance at 2 GHz and 8.2 GHz with different "d" values. After loading the human body model, it can be seen that the radiation pattern of the antenna changes from omnidirectional to directional (Figure 8b,e). In addition, the gain and efficiency increase as the "d" increases, as can be seen in Table 3. When the separation distance "d" is 2 mm, the gain at 2 and 8.2 GHz drops significantly, which might be the results of the human tissue absorbing and radiating electromagnetic waves. Generally, the closer the distance, the stronger the effect. Taken together, at a separation distance of 5 mm, the impact of the human tissue model on the antenna is within an acceptable range, the antenna's front-to-back ratio (FBR) is high, and its gain, efficiency and SAR level meet the design requirements. To evaluate the antenna's actual radiation performance while worn, we conducted a reflection coefficient test at a distance of 5 mm from the antenna to the human body, as shown in Figure 8f. Obviously, the human body has little impact on the antenna radiation performance, indicating that the antenna maintains dual-frequency resonance and high impedance matching in the near-human body test.

The results above demonstrate that the designed antenna not only has good omnidirectional radiation characteristics and broadband matching performance, but it also performs well in terms of conformality and durability, proving its feasibility and practicability as an antenna for wearable devices.

On the whole, the antenna proposed in this work has the following advantages. First, the antenna is paper based and adopts copper materials, which is inexpensive, lightweight and ecologically friendly. It will not form electronic waste and cause pollution to the environment after being discarded. Burning it will only leave some non-toxic and harmless inorganic substances. Second, the antenna operates in the WBAN and X uplink bands, making it suitable for applications in medical monitoring and wearable medical devices. Third, the antenna presented in this study does not included any additional structures like high impedance surface (HIS),[53] artificial magnetic conductor (AMC),[54] and electromagnetic band gap (EBG),[55] it simplifies the design while maintaining acceptable SAR values. It also has a higher aspect ratio than other antennas in design and is easier to conform in the X-axis. These features enable the antenna a competitive candidate for wearable wireless electronic applications.

5. Conclusion

A dual-band wearable antenna is designed and fabricated on photopaper for wearable applications utilizing a screen-printable and plasma-sintered conductive copper paste. The properties of the photopaper substrate and copper paste were investigated thoroughly to help with antenna design and printing. The paste shows good screen-printability and excellent film-forming capability on photopaper substrates, and it can produce highly conductive patterns with an efficient plasma sintering process. The developed antenna is inexpensive, lightweight and ecologically friendly, and it operates in the desired WBAN and X uplink bands. Both simulation and test results demonstrate that the antenna not only has good dual-frequency resonance characteristics, such as good radiation properties and broadband matching performance, but it also performs well in terms of conformality and shows acceptable SAR values on the body. The work could potentially pave the way for low-cost, environment-friendly paper-based wearable wireless electronics.

Supporting Information

Supporting Information is available from the Wiley Online Library or from the author.

Acknowledgements

This work was financially supported by the Liaoning Technical University (Grant No. 21-1039) and the China Scholarship Council (CSC, No. 202308210202). It was completed in the Liaoning Key Laboratory of Radio Frequency and Big Data for Intelligent Applications and the framework of the Joint Lab GEN_FAB.

Conflict of Interest

The authors declare no conflict of interest.

Data Availability Statement

The data that support the findings of this study are available from the corresponding author upon reasonable request.

Keywords

antennas, copper paste, paper substrate, plasma sintering, wearable electronics

Received: July 16, 2024
Revised: September 13, 2024
Published online: October 25, 2024

[1] S. K. Koul, R. Bharadwaj, *Wearable antennas and body centric communication: present and future*, vol. 787, Springer Nature, **2021**.
[2] P. S. Hall, Y. Hao, *Antennas and Propagation for Body-Centric Wireless Communications*, Artech house, **2012**.
[3] Z. H. Jiang, Z. Cui, T. Yue, Y. Zhu, D. H. Werner, *IEEE Trans. Biomed. Circ. Syst.* **2017**, *11*, 920.
[4] U. Ali, S. Ullah, B. Kamal, L. Matekovits, A. Altaf, *IEEE Access* **2023**, *11*, 14458.
[5] S. N. Mahmood, A. J. Ishak, T. Saeidi, H. Alsariera, S. Alani, A. Ismail, A. C. Soh, *Progr. Electromagnet. Res. B* **2020**, *89*, 1.
[6] S. R. Zahran, M. A. Abdalla, A. Gaafar, *IET Microw. Antenn. Propag.* **2019**, *13*, 1219.
[7] Y. Xu, Q. Fei, M. Page, G. Zhao, Y. Ling, S. B. Stoll, Z. Yan, *Iscience* **2021**, *24*, 102736.
[8] Y. Khan, A. Thielens, S. Muin, J. Ting, C. Baumbauer, A. C. Arias, *Adv. Mater.* **2020**, *32*, 1905279.
[9] J. Wiklund, A. Karakoç, T. Palko, H. Yiğitler, K. Ruttik, R. Jäntti, J. Paltakari, *J. Manuf. Mater. Process.* **2021**, *5*, 89.
[10] A. A. Gheethan, D. E. Anagnostou, A. Amert, K. W. Whites, in *2009 Flexible Electronics & Displays Conference and Exhibition*, IEEE, **2009**, pp. 1–5.

[11] G. Shaker, S. Safavi-Naeini, N. Sangary, M. M. Tentzeris, *IEEE Antenn. Wireless Propag. Lett.* **2011**, *10*, 111.
[12] T. Leng, X. Huang, K. Chang, J. Chen, M. A. Abdalla, Z. Hu, *IEEE Antenn. Wireless Propag. Lett.* **2016**, *15*, 1565.
[13] H. P. Phan, T.-P. Vuong, P. Benech, P. X. P. Borel, A. Delattre, in *2017 11th Europ. Conf. Antenn. Propag. (EUCAP)*, IEEE, **2017**, pp. 2168–2171.
[14] J. M. Gonzalez-Perez, L. Marnat, A. Shamim, in *2018 12th Europ. Conf. Antenn. Propag. (EUCAP)* **2018**, pp. 82–83.
[15] M. T. Islam, T. Alam, I. Yahya, M. Cho, *Sensors* **2018**, *18*, 4212.
[16] H. F. Abutarboush, A. Shamim, *IEEE Antenn. Wireless Propag. Lett.* **2018**, *17*, 1648.
[17] M. Shyam, N. Pavithra, P. Priyadarshini, in *2022 2nd Int. Conf. Technol. Adv. Computat. Sci. (ICTACS)*, IEEE, **2022**, pp. 396–402.
[18] H. F. Abutarboush, *Alexandria Eng. J.* **2022**, *61*, 6349.
[19] A. Rida, L. Yang, M. M. Tentzeris, in *2007 IEEE Antenn. Propag. Soc. Int. Symp.*, IEEE, **2007**, pp. 2749–2752.
[20] X. Li, J. Sidén, H. Andersson, T. Schön, *IEEE J. Radio Freq. Identif.* **2018**, *2*, 118.
[21] S. Kanaparthi, V. R. Sekhar, S. Badhulika, *Extreme Mech. Lett.* **2016**, *9*, 324.
[22] S. Merilampi, L. Ukkonen, L. Sydänheimo, P. Ruuskanen, M. Kivikoski, *Int. J. Antenn. Propag.* **2007**, 090762.
[23] P. V. Nikitin, S. Lam, K. Rao, in *2005 IEEE Antenn. Propag. Soc. Int. Symp.*, IEEE, **2005**, pp. 353–356.
[24] H. Koga, T. Inui, I. Miyamoto, T. Sekiguchi, M. Nogi, K. Suganuma, *RSC Adv.* **2016**, *6*, 84363.
[25] A. Mansour, N. Shehata, B. Hamza, M. Rizk, *Int. J. Antenn. Propag.* **2015**, 845042.
[26] C. Baytöre, E. Y. Zoral, C. Göçen, M. Palandöken, A. Kaya, in *2018 28th International Conference Radioelektronika (RADIOELEKTRONIKA)*, IEEE, **2018**, pp. 1–6.
[27] K. Janeczek, G. Kozioł, T. Serzysko, M. Jakubowska, in *3rd Electr. Syst. Integrat. Technol. Conf. ESTC*, IEEE, **2010**, pp. 1–5.
[28] K. Janeczek, A. Młożniak, G. Kozioł, A. Araźna, M. Jakubowska, P. Bajurko, in *Photon. Appl. Astron. Commun. Industry, High-Energy Phys. Experim. 2010*, SPIE, **2010**, pp. 398–404.
[29] D.-Y. Shin, Y. Lee, C. H. Kim, *Thin Solid Films* **2009**, *517*, 6112.
[30] P. Karthik, S. P. Singh, *RSC Adv.* **2015**, *5*, 63985.
[31] W. Li, Q. Sun, L. Li, J. Jiu, X.-Y. Liu, M. Kanehara, T. Minari, K. Suganuma, *Appl. Mater. Today* **2020**, *18*, 100451.
[32] X. Zeng, P. He, M. Hu, W. Zhao, H. Chen, L. Liu, J. Sun, J. Yang, *Nanoscale* **2022**, *14*, 16003.
[33] S. Wünscher, R. Abbel, J. Perelaer, U. S. Schubert, *J. Mater. Chem. C* **2014**, *2*, 10232.
[34] H.-S. Kim, S. R. Dhage, D.-E. Shim, H. T. Hahn, *Appl. Phys. A* **2009**, *97*, 791.
[35] J. Kang, J. Ryu, H. Kim, H. Hahn, *J. Electron. Mater.* **2011**, *40*, 2268.
[36] S. Hong, J. Yeo, G. Kim, D. Kim, H. Lee, J. Kwon, H. Lee, P. Lee, S. H. Ko, *ACS Nano* **2013**, *7*, 5024.
[37] H. Lee, D. Lee, J. Hwang, D. Nam, C. Byeon, S. H. Ko, S. Lee, *Opt. Express* **2014**, *22*, 8919.
[38] K. An, S. Hong, S. Han, H. Lee, J. Yeo, S. H. Ko, *ACS Appl. Mater. Interfaces* **2014**, *6*, 2786.
[39] Y. Farraj, A. Smooha, A. Kamyshny, S. Magdassi, *ACS Appl. Mater. Interfaces* **2017**, *9*, 8766.
[40] I. Reinhold, C. E. Hendriks, R. Eckardt, J. M. Kranenburg, J. Perelaer, R. R. Baumann, U. S. Schubert, *J. Mater. Chem.* **2009**, *19*, 3384.
[41] W. Yang, X. Zhao, Z. Guo, H. Sun, E. J. List-Kratochvil, *Sci. Rep.* **2024**, *14*, 11407.
[42] J. Perelaer, B.-J. De Gans, U. S. Schubert, *Adv. Mater.* **2006**, *18*, 2101.
[43] D. Tobjörk, R. Österbacka, *Adv. Mater.* **2011**, *23*, 1935.
[44] S. Sankaralingam, B. Gupta, *IEEE Trans. Instrument. Measur.* **2010**, *59*, 3122.
[45] A. Jabbar, A. Arif, M. Zubair, K. Riaz, M. Q. Mehmood, in *2021 Int. Bhurban Conf. Appl. Sci. Technol. (IBCAST)*, IEEE, **2021**, pp. 942–945.
[46] E. Svanholm, Ph.D. Thesis, Fakulteten för teknik-och naturvetenskap, **2007**.
[47] C. Moore, T. S. Perova, B. J. Kennedy, K. Berwick, I. I. Shaganov, R. A. Moore, in *Opto-Ireland 2002: Opt. Photon. Technol. Appl.*, SPIE, **2003**, pp. 1247–1256.
[48] M. Vishwas, K. N. Rao, A. Phani, K. A. Gowda, R. Chakradhar, *Spectrochim. Acta Part A: Mol. Biomol. Spectr.* **2011**, *78*, 695.
[49] C. Cano-Raya, Z. Z. Denchev, S. F. Cruz, J. C. Viana, *Appl. Mater. Today* **2019**, *15*, 416.
[50] J. Tang, C. H. H. Mak, S. K. Tam, K. M. Ng, *J. Nanopart. Res.* **2021**, *23*, 166.
[51] S. Ma, V. Bromberg, L. Liu, F. D. Egitto, P. R. Chiarot, T. J. Singler, *Appl. Surf. Sci.* **2014**, *293*, 207.
[52] S. Wünscher, S. Stumpf, A. Teichler, O. Pabst, J. Perelaer, E. Beckert, U. S. Schubert, *J. Mater. Chem.* **2012**, *22*, 24569.
[53] Y.-S. Chen, T.-Y. Ku, *IEEE Antenn. Wireless Propag. Lett.* **2015**, *15*, 1144.
[54] M. Yadav, M. Ali, R. Yadav, *Int. J. Microw. Wireless Technol.* **2023**, *15*, 1514.
[55] P. Sambandam, M. Kanagasabai, S. Ramadoss, R. Natarajan, M. G. N. Alsath, S. Shanmuganathan, M. Sindhadevi, S. K. Palaniswamy, *IEEE Antenn. Wireless Propag. Lett.* **2019**, *19*, 228.